





Mullite photonic glasses with exceptional thermal stability for novel reflective thermal barrier coatings

Alberto Gomez-Gomez^{1,*} , Diego Ribas Gomes¹, Benedikt F. Winhard¹, Laura G. Maragno¹, Tobias Krekeler², Martin Ritter², and Kaline P. Furlan^{1,*} 

¹ Hamburg University of Technology, Institute of Advanced Ceramics, Integrated Materials Systems Group, 21073 Hamburg, Germany

² Hamburg University of Technology, Electron Microscopy Unit, 21073 Hamburg, Germany

Received: 21 April 2023

Accepted: 5 August 2023

© The Author(s), 2023

ABSTRACT

Thermal barrier coatings are essential materials systems for insulating and protecting substrates exposed to high temperatures. In such systems, the heat transfer has three possible paths: conduction, convection and irradiation. The higher the operating temperature, the more important it is to control or protect against the radiative component, since the radiative heat flux becomes non-negligible. The radiation can be controlled by the use of ceramic-based photonic nanostructures, namely photonic crystals and photonic glasses, creating so-called reflective thermal barrier coatings. In this work, mullite inverse photonic glasses (PhG) have been produced by thermally induced reaction on sol-gel-based silica structures coated with nanometric films of Al₂O₃ by atomic layer deposition. The conversion to mullite was carried out following a two-stage heat-treatment. The pre-annealing associated with the further mullite formation results in an excellent structural stability of these PhGs up to 1500 °C, being able to retain their high reflectivity in the near infrared range. Therefore, this structure can be considered for next-generation reflective thermal barrier coatings.

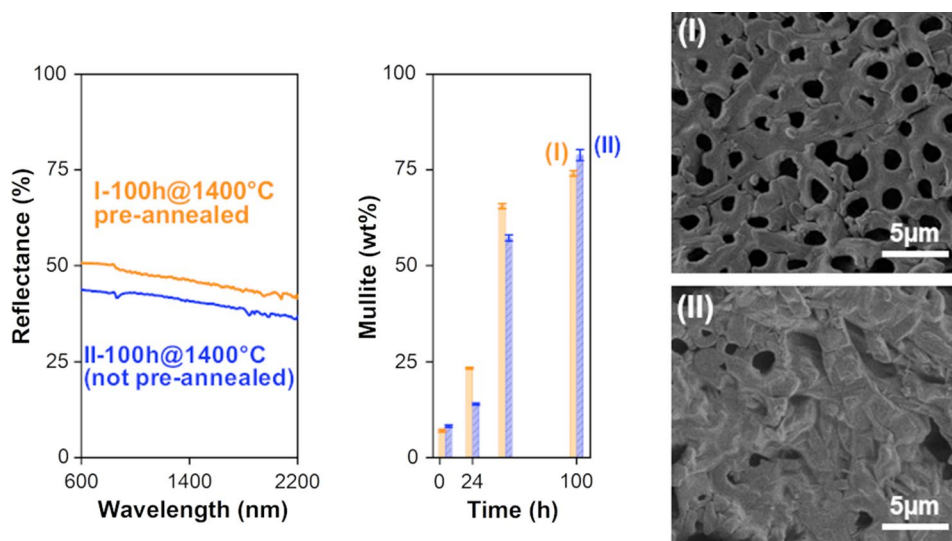
Handling Editor: Maude Jimenez.

Address correspondence to E-mail: alberto.gomez@tuhh.de; kaline.furlan@tuhh.de

<https://doi.org/10.1007/s10853-023-08844-2>

Published online: 21 August 2023

GRAPHICAL ABSTRACT



Introduction

In certain high-temperature applications, such as combustion chambers or gas turbines, thermal barrier coatings (TBC) have become essential for insulating and protecting metallic substrates. These coatings ensure that the maximum temperatures of the superalloy components remain significantly lower than those of the gas stream, resulting in increased component lifetime [1]. To illustrate this, reducing the peak temperature by just 15 °C can potentially double the lifespan of turbine blade superalloys [2]. Typically, these structures are made of yttria-stabilized zirconia (YSZ) since this material offers an excellent combination of thermal and mechanical properties, including high thermal expansion coefficient, low thermal conductivity and high thermal shock resistance [3, 4].

The main goal for next-generation advanced engines is to increase fuel efficiency, which can be accomplished by increasing the turbine inlet gas temperature. This presents challenges in terms of both materials and structure of the TBCs, which are expected to operate at temperatures approaching 1600 °C [5]. At such elevated temperatures the radiative heat flux becomes non-negligible. For example, in a conventional TBC at 1200 °C, the radiative heat transfer is estimated to be about 20% of the conduction heat transfer [6, 7], and this proportion further increases at higher temperatures. Taking the blackbody emission spectrum as an example (Fig. 1), the emissive power

grows exponentially with the fourth power of the temperature according to the Stefan–Boltzmann law. This radiative power is concentrated within the wavelength range of 0.5–5 μm, especially in the near infrared (NIR) range (0.78–3 μm).

In recent years, several works on TBCs have focused on optimising the reflectivity of these structures in the NIR region to limit the radiative heat flow to the superalloy components. In conventional TBCs, mainly produced by air plasma spraying (APS) or electron beam physical vapor deposition (EB-PVD), this optimization comprises increasing the density of scattering defects (pores and microcracks) or modifying their arrangement within the coating to increase the photon scattering efficiency and overall reflectivity of the TBCs [8–13]. Significant progress has also been achieved in the development of reflective thermal barrier coatings (rTBC) based on photonic crystal structures (PhC). These PhCs are composite media consisting of materials with different dielectric constants arranged periodically. Their long-range order structure enables interaction with electromagnetic radiation, leading to the reflection of incident radiation within a specific wavelength range. The position and width of these strong reflection bands is determined mainly by the periodicity constant and the refractive index contrast. Ceramic-based opals, face centered cubic (FCC) arrangements of monodisperse ceramic micro-spheres, serve as a complex three-dimensional PhC example proposed as rTBCs [7]. Similarly, inverse

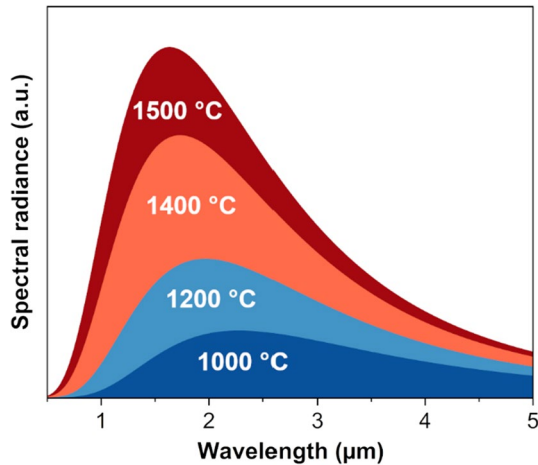


Figure 1 Spectral radiance emitted by a blackbody at 1000 °C, 1200 °C, 1400 °C and 1500 °C

opals, formed by enclosing spherical pores with large range order arrangement in a ceramic matrix, have also proven their potential for such applications [7, 14–16].

One of the main drawbacks for the application of PhCs as rTBCs is their narrow reflection band. To overcome this limitation, Lee et al. proposed multi-stack PhC structures with different lattice constants, so that their reflection band would be located in different photon wavelengths, and thereby achieve a broadband reflection [7]. Although these structures would theoretically be able to reflect over 80% of the radiation in the 1–5 μm range, their fabrication is a challenge and often results in a significant density of undesired defects and cracks, which reduce their reflection efficiency [17, 18].

Alternatively, photonic glasses (PhGs), consisting of the same building blocks as PhCs but possessing short-range rather than long-range order, exhibit an omnidirectional broadband reflection due to the multiple scattering of radiation at wavelengths comparable to the particle/pore diameter [19]. Compared to other solutions for rTBCs, PhGs have the clear advantage of a simpler fabrication route while reaching even higher reflectivity values than multi-layered PhCs [19–23]. Moreover, while defects in the long-range order of the PhCs impair their photonic behaviour, the absence of long-range order in PhGs makes them less sensitive to structural defects. In addition, PhG-based rTBCs exhibit a remarkably low thermal conductivity, even lower than conventional TBCs of the same material produced through APS or EB-PVD methods [19, 20].

The fabrication of photonic crystals and glasses by self-assembly techniques is widely documented. Particularly, the fabrication of inverse PhGs typically involves infiltrating a sacrificial self-assembled template through sol–gel infiltration, chemical vapor deposition or atomic layer deposition (ALD). The final photonic inverse structure is then obtained after template removal, e.g. through a burn-out treatment or chemical etching [14–18, 21, 23–27].

In addition, an increase in the operating temperature of TBCs is a challenge for the materials used in these coatings. For instance, the maximum temperature at which YSZ can operate continuously is limited to about 1200 °C. Beyond this temperature, sintering and phase transformations compromise the integrity of the coating [1, 4, 28, 29]. Besides YSZ, the application of other ceramics as TBC has also been subject to study. In recent years, there has been a growing interest in TBCs based on rare-earth hafnates and rare-earth oxide stabilised cubic hafnia, which are capable of maintaining the structural stability of these systems above 1500 °C [30, 31]. However, the use of these materials in highly porous photonic structures for rTBCs is still under development. On the other hand, another proposed material for TBCs is mullite, characterized by a molar composition ranges from $3\text{Al}_2\text{O}_3 \cdot 2\text{SiO}_2$ (3:2 mullite) to $2\text{Al}_2\text{O}_3 \cdot \text{SiO}_2$ (2:1 mullite) [14, 16, 32, 33]. In contrast to YSZ, mullite has high thermal-stability and does not exhibit phase transformation from room temperature to temperatures above 1500 °C. In addition, mullite exhibits low thermal conductivity as well as chemical-, thermal shock- and creep-resistance [34, 35].

In this work, mullite inverse PhGs with a strong reflectivity in the NIR range and high structural stability at high-temperature were produced. For the deposition of the ceramic phases, a combination of sol–gel infiltration and ALD was investigated as a potential manufacturing method for PhG fabrication. This combined approach achieved a high filling fraction of the sacrificial template, which positively influenced the thermal stability and NIR reflectivity of these PhGs. In addition, the effect of a pre-annealing at temperatures below the mullite formation on the structural stability of these PhGs when subsequently exposed to higher temperatures has been investigated. In comparison to traditional TBCs or other photonic structures proposed for this application, the mullite inverse PhGs developed in this work show a superior

thermal-stability, retaining the photonic structure and reflectivity up to 1500 °C.

Materials and methods

Materials and samples preparation

Initially, direct PhG coatings made from polystyrene (PS) particles ($3.03 \pm 0.09 \mu\text{m}$, microParticles GmbH) were deposited onto sapphire substrates (A-oriented surface, $25 \times 30 \times 0.53 \text{ mm}^3$, Crystec GmbH). For the deposition, 300 μl of aqueous suspensions with a concentration of 20 $\text{mg}\cdot\text{ml}^{-1}$ of PS particles were drop-casted within a Teflon ring fixed to the sapphire substrate. Prior to the PS template deposition, the substrate surfaces were oxygen-plasma cleaned and activated for 20 min (Polaron PT7160, Quorum Technologies). The samples were then air-dried at room temperature for at least 24 h, partially covered with a plastic vessel to allow air circulation.

To enhance the mechanical stability of the polymeric PhG templates, they were heated in an air Muffle furnace for 3 h at 110 °C before undergoing vertical convective infiltration (VCI). For the VCI process, a hydrolysed solution of tetraethylorthosilicate (TEOS, $\geq 99.0\%$, Sigma-Aldrich), ethanol and 0.10 M HCl was prepared with a weight ratio of 1:6:1. Each sample was vertically immersed in a Teflon beaker containing 0.450 ml of this TEOS solution diluted in ultrapure water to a total volume of 50 ml. The beakers were placed in a humidity chamber (VTR 5022, Heraeus Instruments) maintained at 60 °C and a high relative humidity (90–100%) for 7 days. This technique is based on the flow-controlled vertical deposition (FCVD) method developed by Zhou et al. [26], who controlled the velocity of the dropping liquid surface by slowly withdrawing the solution with a peristaltic pump. In the VCI method, the dropping velocity of the liquid surface is directly related to the evaporation rate of the solvent, which in turn depends on the temperature and relative humidity in the chamber.

Once the PS template was infiltrated with silica, the PS particles were burnt-out in an air Muffle furnace for 30 min at 500 °C (heating rate of $0.4 \text{ }^\circ\text{C}\cdot\text{min}^{-1}$) to generate silica inverse PhG structures. The deposition of alumina was carried out using ALD in a custom-made reactor (Hamburg University of Technology, TUHH) at 95 °C. Trimethylaluminium (TMA, Sigma Aldrich) and deionized water were used as precursors,

and nitrogen as carrier gas ($2 \text{ NI}\cdot\text{h}^{-1}$). The pulse, exposure, and pump times for TMA and water precursors in each of the 1830 ALD cycles used for alumina deposition were set at 0.06/15/90 and 0.12/15/90 s, respectively. To measure the thickness of the alumina films, reference silicon wafers were first placed within the reactor close to the silica PhGs during the deposition, and then analysed by spectroscopic ellipsometry with an incident angle of 70° (SE-2000, Semilab). The resulting growth per cycle (GPC) and refractive index (n) were 1.64 Å and 1.65 (at 632.8 nm), respectively, which are well align with previously-reported results [14, 27].

Thermal treatments and characterization

Silica-alumina PhGs underwent a two-stage heat-treatment using a resistive Muffle furnace:

- An initial stage at 850 °C for 24 h to promote diffusion and thus contribute to the compositional homogenisation of the PhG before mullite conversion, henceforth referred to as “pre-annealing”. Mullite formation temperatures in the range of 900–1000 °C have been reported for highly homogeneous silica-alumina structures [14, 15, 36–38]. To promote homogenisation through diffusion while preventing early formation of mullite, the temperature for this stage was set at 850 °C. The total dwell time of 24 h was determined based on the calculations for estimating the diffusion of aluminium from the ALD-deposited alumina layer towards the silica core of these PhGs, assuming diffusion in all directions (Figure S1).
- High-temperature heat-treatments at 1000 °C, 1200 °C and 1400 °C, with cumulative times up to 100 h. These temperatures were chosen to align with the working range of TBCs, as well as to enable the comparison with previous works [4, 5, 8, 17, 19–23].

Furthermore, the impact of the first stage on the thermal-stability of these PhGs was evaluated. A comparison was made between sequentially heat-treated samples for a total of 4, 24, 48 and 100 h at 1400 °C, both with and without pre-annealing. Additional heat-treatments conducted in this work are summarized in Table 1. The heating rate of all individual heat-treatments was set at $5 \text{ }^\circ\text{C}\cdot\text{min}^{-1}$.

Table 1 Summary of the heat-treatments that were sequentially performed on the samples analysed in this work

Sample	Pre-annealing	Consecutive high-temperature heat-treatment			
		1 st	2 nd	3 rd	4 th
I	24 h-850 °C	4 h-1000 °C	20 h-1000 °C	4 h-1500 °C	20 h-1500 °C
II	24 h-850 °C	4 h-1200 °C	20 h-1200 °C	–	–
III	24 h-850 °C	4 h-1400 °C	20 h-1400 °C	24 h-1400 °C	52 h-1400 °C
IV	–	4 h-1400 °C	20 h-1400 °C	24 h-1400 °C	52 h-1400 °C

The structural stability of these ceramic PhGs were assessed before and after each heat-treatment. For this purpose, cross sections and top surfaces of the PhGs were examined using scanning electron microscopy (SEM, Zeiss Supra 55 VP). After each heat-treatment, hemispherical reflectance spectra of the PhGs were collected in the wavelength range of 0.6–2.2 μm using a UV–Vis–NIR spectrometer with an integrating sphere module (Perkin-Elmer, Lambda 1050). The thickness of these regions was determined by examining their cross-section with SEM. To identify the microstructural phases of the heat-treated PhGs, grazing incidence X-ray diffraction analysis was employed, utilizing Cu K α radiation (Bruker AXS D8 Advance, Bruker). The incident angle was set at 0.5°, with a step size of 0.01° and step time of 5 s. XRD patterns from the Crystallography Open Database (COD) were used for the phase identification. Rietveld refinement was performed using MAUD (Materials Analysis Using Diffraction) software to compute the phase fractions. Scanning transmission electron microscopy (STEM) images and energy dispersive X-ray (EDS) spectral maps were collected using a FEI/Thermo Fisher Scientific Talos F200X equipped with a FEI Super-X G2 EDS detector operating at 200 keV. In order to prepare STEM samples, the heat treated PhGs were crushed into fine particles, dispersed in ethanol by ultrasonication and subsequently deposited onto carbon-coated grids.

Results and discussion

For the fabrication of PhCs and PhGs of spherical particles, self-assembly techniques are popular and low-cost methods [14, 15, 17, 20, 21, 39–41]. In this work, the PhG structure of PS particles was produced by drop-casting technique. Although drop-casting of stable colloids consisting of monodispersed particles usually results in the formation of PhCs, polydispersity

or colloidal instability can introduce disorder in the particle arrangement [39, 42]. Particularly, when using large particles like the ones used in this work, the effect of gravity leads to quick sedimentation of the particles in a random arrangement [20], forming a photonic glass structure. Small regions with an ordered particle arrangement were eventually observed in the bottommost layers of the films. However, no discernible feature associated to PhCs were found in the reflectance spectra. A similar observation was described by Do Rosário et al., who reported that a few layers with ordered arrangement had no relevant influence in the photonic properties of YSZ-PhGs [21].

Once the PhGs templates were deposited on the substrate and dried, the subsequent step involved their infiltration to produce the ceramic inverse PhG structure. ALD is a technique capable of depositing uniform coatings on structures with a high aspect ratio and an extraordinary control over thickness. Besides, the deposition of mullite by ALD supercycles has been reported by our group with promising results regarding the thermal-stability of inverse photonic crystals [14]. However, the template infiltration by this technique is limited, since it relies on the accessibility of the gaseous precursors to the to-be-coated surfaces. In self-assembled PhCs and PhGs templates, the interstitial voids of the structure are eventually closed, preventing further infiltration and thus restricting the shell thickness and overall ceramic structure/air pore ratio [15]. It should be noted that the infiltration of these structures plays an important role in the structural stability of the PhGs at high-temperatures. In one of our previous works with ALD-based Al₂O₃ inverse PhCs, it was observed that samples with a thicker shell (higher filling fraction) presented a better retention of their photonic structure when exposed to high-temperatures [27].

In contrast to ALD, the VCI technique selected in this work is able to achieve a high filling fraction despite being based on a sol–gel process, as shown in

Fig. 2a. This approach is inspired by the FCVD method developed by Zhou et al., who explained how the slow speed of the dropping liquid surface sustains capillary forces in the emerged areas near the liquid surface [26]. According to their findings, the slower the

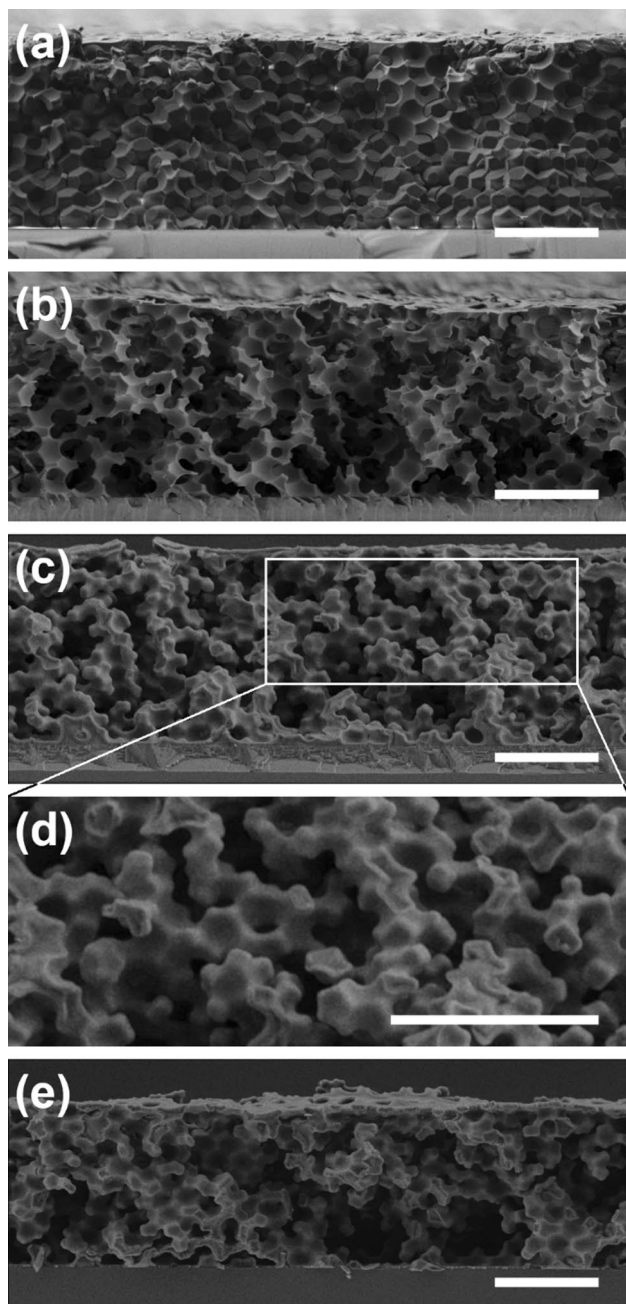


Figure 2 Cross-section SEM images of **a** silica-infiltrated photonic glass (PhG), **b** inverse silica PhG after the PS template removal, **c**, **d** alumina-silica PhG after the ALD process and **e** after pre-annealing at 850 °C for 24 h. Scale bars correspond to 10 μm

speed of the liquid surface, the higher filling fraction is achieved due to the extended contact time between the PS template and the TEOS solution. Consequently, the authors reported that a dropping velocity of $0.5 \mu\text{m}\cdot\text{s}^{-1}$ resulted in a filling fraction exceeding 80% of the hypothetical fully dense silica matrix. In this work, the speed of the meniscus formed close to the PS template was $\sim 0.1 \mu\text{m}\cdot\text{s}^{-1}$, lower than that used by Zhou et al., to aim for the highest-possible filling fraction.

Upon the removal of the polymeric template (Fig. 2b), the pore inter-connectivity allowed the deposition of the aluminium oxide by ALD. In this scenario, the ALD's advantages position it as an ideal choice for preserving the porous inverse PhG structure unaltered while increasing the shell thickness, i.e. the ceramic filling fraction. The thickness of the alumina layer can be estimated by considering the ratio between the required alumina volume for achieving the mullite composition and the specific surface area of the inverse PhG. In addition, the volume of alumina can be calculated based on the specific volume of silica in the structure, the expected molar ratio of alumina to silica in mullite, as well as the compound's molar masses and densities. As an initial approximation for the specific surface area, we employed an estimation derived from an inverse opal with FCC lattice formed by pores of the same size ($\sim 3 \mu\text{m}$). Assuming a lattice parameter $a = 2^{3/2} \times r$, where r is the pore radius, and 4 macropores per unit cell, this inverse opal structure has a specific surface area of $2.7 \text{ m}^2\cdot\text{cm}^{-3}$. Taking into account the packing fraction in an ideal opal (0.74), an alumina layer of around 200 nm thickness would be required.

Compared to opals, the inverse PhGs produced in this work have a lower estimated packing fraction (0.56 [43]), resulting in a lower number of pores per volume. Consequently, these photonic glasses exhibit not only a lower specific surface area, but also a higher volume fraction of silica. Therefore, a larger volume of alumina may be required to potentially achieve a full conversion to a mullite phase. However, the ALD infiltration of these structures is limited due to the need for pore interconnection. To ensure successful ALD deposition on the structure without closing the pores, the alumina layer thickness was restricted to 300 nm. The cross-section analysis of the structures after the ALD process confirms that the thickening of the struts does not completely close the pores of the structure (Fig. 2d). In a previous work conducted by our group [27], we have shown that the structural stability of

alumina PhCs at high temperature was closely linked to the sintering of the structure. Regions with more pronounced curvature were associated with enhanced sintering and consequent degradation of the photonic structure. Such regions with high curvature are less pronounced in this study's mullite PhGs (see Fig. 2d), which we hypothesize to be a contributing factor for their higher thermal-stability, discussed in the next section.

Photonic properties and thermal-stability

The characteristic broadband omnidirectional reflection of inverse PhGs is based on Mie resonances [44, 45]. These interactions with electromagnetic radiation are highly dependent on the pore size and the refractive index contrast between the dielectric material of the structure and the medium inside the pores. Thereby, retaining the integrity of the photonic structure is essential to preserve their “radiation reflection capability”. At elevated temperatures, however, keeping the structural stability of such highly-porous ceramic structures remains a challenge. Phenomena such as phase transformations, grain growth or densification can distort the photonic structures.

Furthermore, the total thickness of the PhGs is another key parameter in determining the photonic properties of these structures. To ensure comparability of the reflection spectra for a specific inverse PhGs after each consecutive heat treatment, they were always recorded at the same area of each sample. Upon completion of the characterization of the samples, the thickness of these particular regions was determined by SEM analysis. The results are presented in Table S1. Except for the sample treated directly at 1400 °C, which will be discussed later, all PhGs exhibited an average thickness of about 20 µm. To provide a clear overview, Fig. 3 summarises in a flowchart the different stages analysed in the discussion of the results.

The reflection spectra of these mullite inverse PhGs were compared initially after a 4 h heat-treatment at temperatures ranging from 1000 to 1400 °C (Fig. 4a). Specifically, the sample treated at 1000 °C showed no changes in morphology (Figs. 2, S2 and S3), nor mullite crystallisation, as will be discussed later. For this reason, this sample was subsequently treated at 1500 °C, and these results were included in the comparison. All the inverse PhGs showed high reflectivity values (50–60%) across the entire

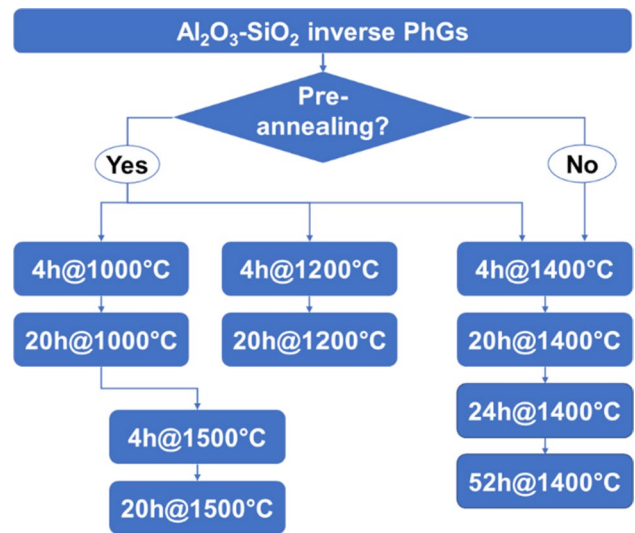


Figure 3 Flowchart of the high-temperature heat-treatments. Scanning electron microscopy (SEM), X-ray diffraction (XRD), and reflectance spectra were analysed after each high-temperature heat-treatment

analysed wavelength range, corresponding to the region of highest blackbody radiation emission at the temperatures of interest. It is noteworthy that these reflectivity values are achieved despite the relatively thin thickness of about 20 µm of the mullite inverse PhGs.

In order to be suitable for high-temperature applications, these structures must demonstrate high thermal-stability over extended periods of time. Figure 4b presents the reflectance spectra of mullite inverse PhGs heat-treated for a total of 24 h at different temperatures. Interestingly, after 24 h of heat-treatment, the sample treated at 1500 °C retained its high reflectivity value even better than the inverse PhG exposed at 1400 °C. This observation is further discussed ahead in terms of mullite formation.

Compared to other types of TBCs, the reflective TBCs based on mullite inverse PhGs exhibit similar or higher reflectivity than alternative solutions based on inverse PhGs or more traditional TBCs deposited by EBPVD (Fig. 5a). While other material systems such as plasma-sprayed TBCs or refractive TBCs based on direct PhG structures demonstrate superior reflectivity in absolute values, these results are achieved at coating thicknesses between 5 and 10 times higher than the mullite inverse PhGs (Fig. 5b). In a direct comparison with the YSZ inverse PhGs proposed by Do Rosario et al. [21, 23], our mullite

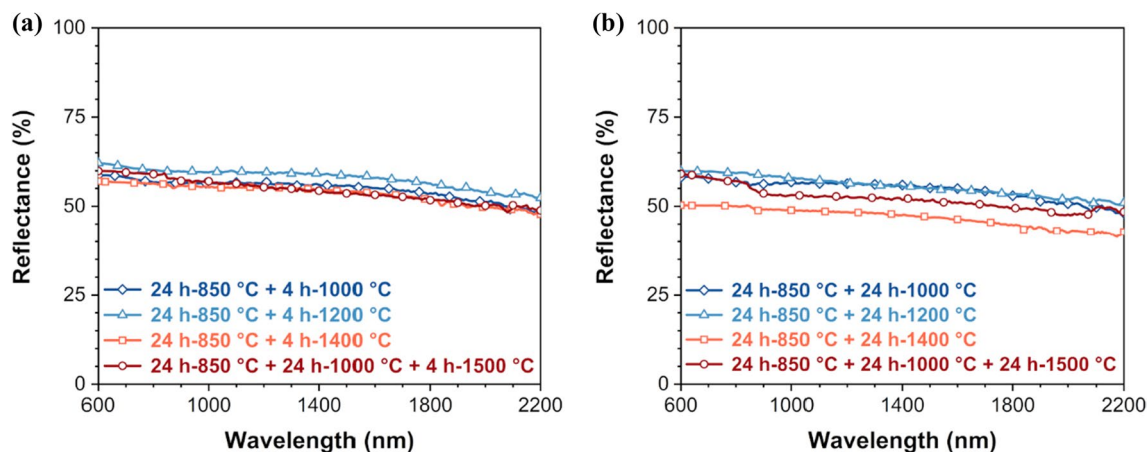


Figure 4 Reflectance spectra of PhGs pre-annealed and heat-treated at 1000 °C, 1200 °C, 1400 °C and 1500 °C for **a** 4 h and **b** 24 h. The sample treated at 1500° was previously heat-treated for 24 h at 1000 °C

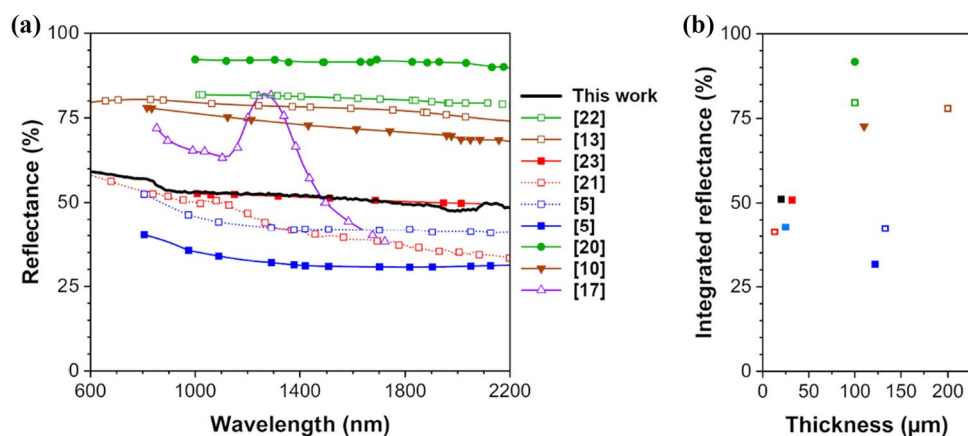


Figure 5 a Reflection spectra of mullite inverse PhG heat-treated for 24 h at 1500 °C, YSZ direct PhG heat-treated at 1400 °C for 192 h [22], APS YSZ-TBC [13], YSZ inverse PhG with a pore size of 3.2 μm heat-treated at 1200 °C for 120 h [23], YSZ inverse PhG with a pore size of 0.7 μm heat-treated at 1200 °C for 4 h [21], EB-PVD YSZ-TBC heat treated at 950 °C for 20 h (* denotes a YSZ TBC with a 1D PhC structure formed by

multiple layers with different density) [5], ZrO₂ direct PhG [20], APS Gd₂Zr₂O₇-TBC [10], and TiO₂ multi-stacked PhC with the pore sizes of 756 nm (bottom) and 608 nm (top) [17]. **b** Integrated reflectance of the previous coatings in the wavelength range of 1000–2200 nm as a function of the total coating thickness

PhGs showed similar reflectivity in the same wavelength range despite the higher refractive index of YSZ ($n = 2.12$ [4, 19–21, 23]) compared to mullite ($n = 1.65$ [46]). In their work, Do Rosário et al. already observed that the samples with the highest filling fraction exhibited superior reflectivity and thermal stability. In this sense, the mullite PhGs analysed in this work were produced with the aim of achieving a high filling fraction. In contrast, the meso- and microporosity of the nodes and struts in the nanoparticle-based YSZ PhGs reduced their effective

refractive index, which is considered to be one of the reasons for their lower reflectivity compared to mullite PhGs. This emphasizes the advantage of the herein reported processing route combining sol-gel and ALD.

In addition, the high reflectivity of mullite PhGs is maintained even after exposure to 1500 °C, which is clearly surpasses the operating limit of YSZ TBCs. In recent times, significant advancements have been achieved in the development of novel materials for TBCs capable of preserving their structural integrity

at elevated temperatures exceeding 1450 °C. Examples include cubic zirconia/hafnia stabilised with rare-earth oxides such as Gd_2O_3 , Y_2O_3 or Lu_2O_3 [29], oxides with pyrochlore structure such as $\text{Gd}_2\text{Zr}_2\text{O}_7$ [10], or mullite with SiC whiskers [47]. However, up to now, the application of these materials is limited to traditional TBCs and not highly porous photonic structures for rTBCs.

To further analyse the thermal-stability of mullite inverse PhGs, as well as the influence of pre-annealing, consecutive heat treatments were performed at 1400 °C for a total dwell time of 100 h on a pre-annealed and a non-pre-annealed sample (Fig. 6). In order to compare the reflectivity of two different samples after consecutive heat-treatments at 1400 °C, reflectance spectra were normalized based on the maximum value of reflectivity after the 4 h heat-treatment. At that point the samples showed similar absolute reflectivity values (Figure S4).

In the sample directly treated at 1400 °C, a decrease in reflectivity was observed with increasing exposure time (Fig. 6a). This observation was consistent with the SEM analysis conducted on the top surface and cross-section of the mullite PhG (Fig. 7). With prolonged dwell time at high-temperature, the densification of the structure progressed, resulting in the closure of pores on the top surface and the formation of dense regions throughout the coating thickness (Fig. 7a, c, e, g). Although the cracks were not caused by these heat-treatments (they were present after the infiltration step of the polymeric sacrificial templates, Figure S2), widening of the cracks was observed as the densification process progressed. All these changes led to distortion of the initial structure and subsequent deterioration

of the photonic properties. Furthermore, the densification of these porous structures due to sintering explains the reduced film thickness measured on this sample after the heat-treatments, earlier presented.

In contrast, the previously annealed sample retained the PhG photonic structure even after 100 h at 1400 °C (Fig. 7b, d, f, h). Although a reduction in the reflectivity of PhG was observed after the first 24 h, there was no further decrease in the reflectance spectra after 100 h at that temperature. The minor signs of sintering observed in this sample are not comparable with the clear densification found in the non-annealed sample. Nonetheless, some extent of pore closure was observed on the top surface after 48 h (Fig. 7f). This was not spread-out throughout the sample, but only affected a limited number of pores. A similar situation was observed after 100 h (Fig. 7h).

Mullite phase formation

The inverse silica-alumina PhGs were still amorphous prior to the high-temperature heat-treatments (Figure S5). The amorphous nature of the alumina coating is a result of the low temperature of the ALD process [14, 15], while the silica phase was not expected to crystallize into cristobalite at the temperature of the ALD deposition or the pre-annealing treatment. An X-ray diffraction study on sol-gel silica reported the formation of cristobalite from 900 °C onwards, but a fast cristobalite growth was not observed until 1100–1200 °C [48].

Figure 8 shows the diffractograms of the PhGs after the pre-annealing stage and the 4 h heat-treatments

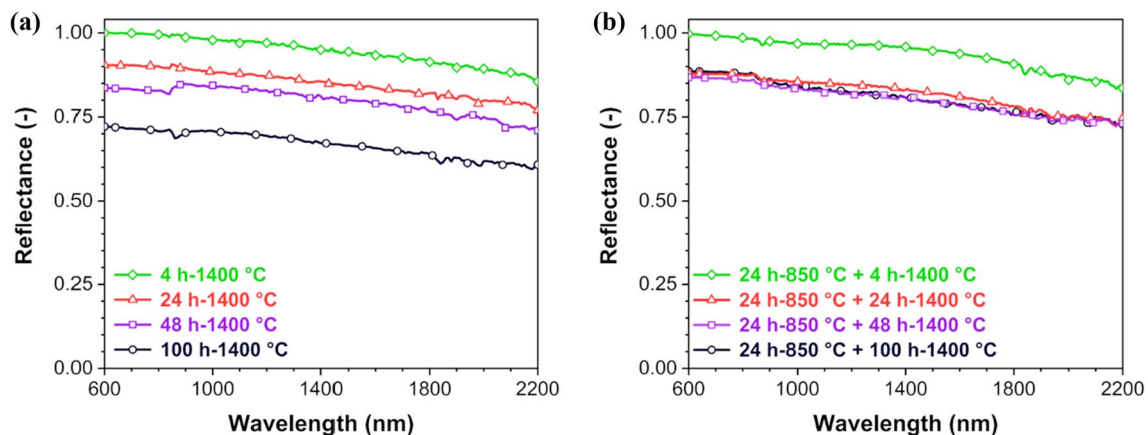
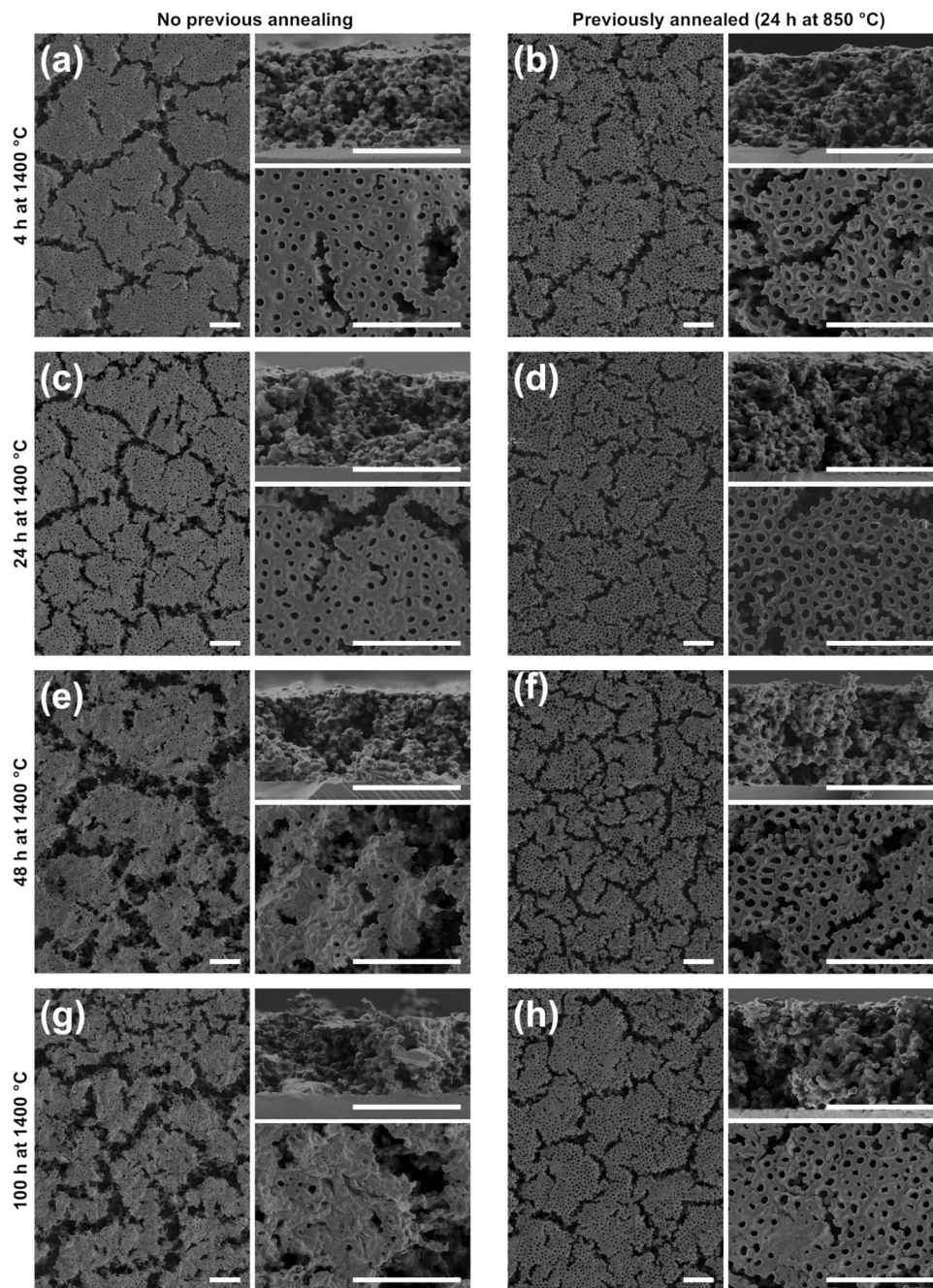


Figure 6 Normalized reflectance spectra of mullite PhGs, **a** directly heat-treated and **b** pre-annealed samples, after heat-treatments at 1400 °C for 4 h, 24 h, 48 h and 100 h

Figure 7 Top surface and cross section views of mullite PhGs heat-treated with (right column) and without (left column) previous heat treatment at 1400 °C for **a, b** 4 h, **c, d** 24 h, **e, f** 48 h and **g, h** 100 h. Scale bars correspond to 20 μm



at different temperatures. After pre-annealing at 850 °C, X-ray diffraction revealed only broad and low intensity peaks, indicating partial crystallization into η -, γ -, δ - and θ -alumina. Similar results were obtained after heat-treatments at 1000 °C, whereas at 1200 °C, sharp and intense peaks associated to α -alumina were clearly identifiable. Mullite formation took place only at temperatures above 1400 °C, a temperature 400–500 °C higher than that observed for

monophasic gels or structures produced by an ALD supercycle, but close to that reported for diphasic gels (1200–1300 °C) and clearly lower than the crystallization temperature of mullite obtained from ceramic powders (1500–1700 °C) [15–17, 34–36, 46].

Minor diffraction peaks associated with cristobalite were only found in the PhGs treated at 1200 °C (Fig. 8 and S6). The absence of cristobalite at lower temperatures agrees with the previous X-ray study

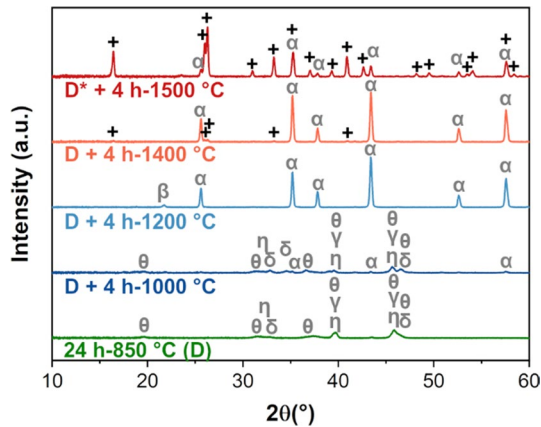


Figure 8 XRD diffractograms of samples pre-annealed at 850 °C for 24 h (indicated as D on the other diffractograms) and subsequently heat-treated at 1000, 1200, 1400 and 1500 °C for 4 h. The sample treated at 1500 °C had previously been exposed to a total of 24 h at 1000 °C in addition to the pre-annealing (indicated as D*). Mullite peaks (COD 9010159) are represented by +, α -alumina (COD 9007634) by α , η -alumina (COD 1101168) by η , γ -alumina (COD 1010461) by γ , δ -alumina (COD 1537011) by δ , θ -alumina (COD 1200005) by θ , and cristobalite (COD 9008110) by β

[48]. On the other hand, at higher temperature, the presence of both mullite and alumina on the surface of amorphous silica particles has been shown to inhibit the crystallization of cristobalite by introducing compressive forces [49, 50]. Furthermore, our previous estimations in regard to sample composition, i.e. sol-gel silica to ALD alumina ratio, leaned towards the alumina-rich range of the mullite phase

diagram so that all silica shall be eventually consumed to form mullite.

In order to analyse the influence of the previous diffusion stage on these structures when they are later exposed to high-temperatures, consecutive heat-treatments were carried out on non-annealed and pre-annealed inverse PhGs at 1400 °C for a total of 100 h (Fig. 9). At this temperature, the formation of mullite was already observed after 4 h.

The results of Rietveld refinement on these diffractograms reveal that mullite formation is enhanced by the pre-annealing stage (Fig. 10), despite the diffractograms' apparent similarity. Particularly, after 24 h at 1400 °C the previously annealed sample exhibited a higher proportion of mullite phase (23 wt.%) compared to the sample directly heat-treated (14 wt.%). This difference was still observed after 48 h of heat-treatment, but both samples reached a mullite content of about 75 wt.% after 100 h. These findings point to the relation between the earlier mullite formation and the improved structural stability in the pre-annealed samples. In comparison, the inverse PhG treated at 1500 °C showed well-advanced mullite formation (above 80 wt.%) after dwell times as short as 4 h and this proportion hardly increased with longer heat-treatments. These observations agree with earlier studies on the dependence of temperature and dwell time on mullite formation [38, 51].

Although the conversion to mullite was clear for these inverse PhGs, diffraction peaks associated with α -alumina were still present. This indicates that the thickness of the deposited alumina layer exceeded

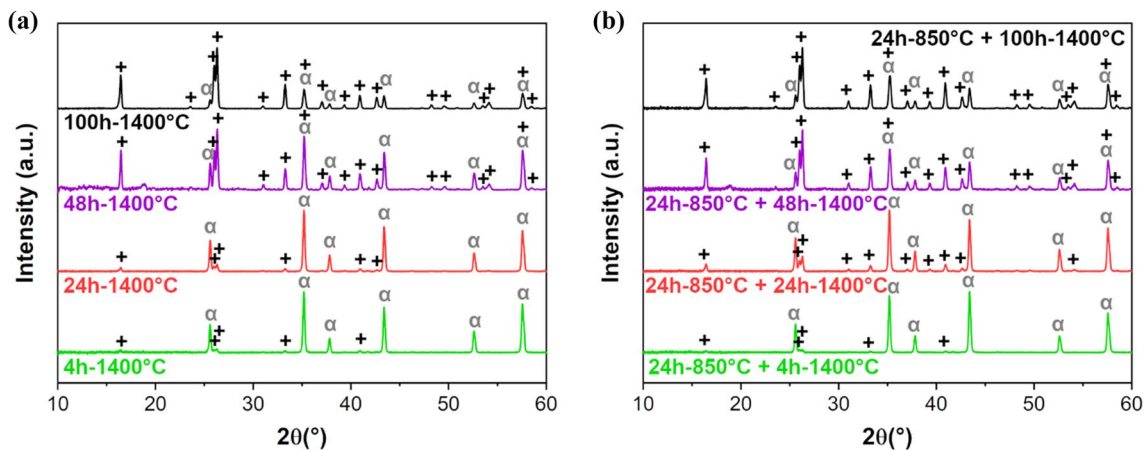


Figure 9 XRD diffractograms of mullite PhGs **a** directly heat-treated and **b** pre-annealed samples, after heat-treatments at 1400 °C for 4 h, 24 h, 48 h and 100 h. Mullite peaks (COD 9010159) are represented by +, α -alumina (COD 9007634) by α

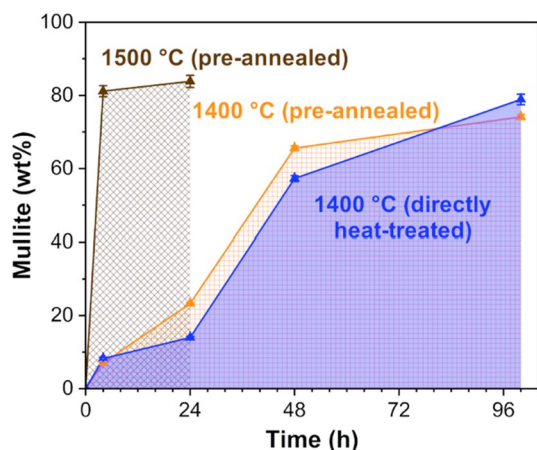


Figure 10 Estimated mullite phase fraction in the inverse PhGs after high-temperature heat-treatments

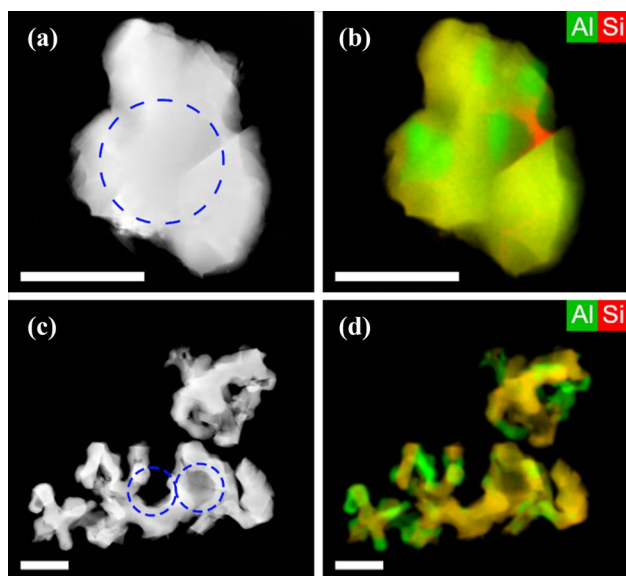


Figure 11 High-angle annular dark-field (HAADF) images and EDS colour maps of **a–b** PhGs directly heat-treated at 1400 °C for 100 h; and **c–d** pre-annealed samples with the same heat-treatment. The dashed circles mark the position previously occupied by the 3 µm PS template spheres. The yellow and green colours denote regions of mullite and alumina, respectively. The composition maps of O, not shown, exhibit a uniform distribution throughout the particles. Scale bars correspond to 3 µm.

the minimum required to achieve a full-conversion to mullite, considering the initial silica content. Future studies aim to determine the optimal film thickness for complete conversion without an excess of alumina phase.

The presence of mullite and excess alumina phases was further confirmed by STEM-EDS maps (Fig. 11). Precise element quantification is challenging due to the large variation in thickness throughout the analysed particles. Nonetheless, the stoichiometry extracted from thin regions was in a good agreement with that of mullite (Figure S10). In one of the directly heat-treated samples (Fig. 11b), areas with above-average Si content were observed, supporting the argument for incomplete homogenization in those samples compared to pre-annealed ones.

These results altogether confirm that mullite formation prevents degradation of the photonic structure at temperatures above 1400 °C. This follows from the extraordinary thermal-stability of mullite compared to the different polymorphic phases of alumina or silica [35]. Thus, our work demonstrates that promoting mullite conversion in nanostructured PhGs is key to enable their use in high temperature applications. In the absence of pre-annealing treatment, the reflectance spectra decreased progressively as the dwell time increased from 4 to 100 h at 1400 °C (Fig. 6).

It should be noted that the cracks resulting from silica-infiltration, visible at the SEM analysis of top surface of PhGs, did not significantly widen during heat-treatments at temperatures above 1000 °C (Fig. 7 and S2). The cracks present in these systems may be seen as an obstacle for their sole application as rTBC, considering that TBCs are also designed to protect against oxidising and corrosive environments. Nonetheless, such mullite inverse PhGs could be a potential addition to conventional TBCs rather than a complete replacement. Their high reflectivity in the NIR range, low thermal conductivity, and structural stability at high-temperature make these PhGs potential candidates for advanced multi-layer rTBC material systems.

Conclusions

Mullite inverse PhGs were produced by heat treatment from nanostructured silica-alumina structures obtained by sol-gel and ALD. These PhGs proved to have an exceptional structural stability at high-temperature, retaining the infrared reflectivity at temperatures above 1400 °C during long times (up to 100 h). These excellent results benefit from the high filling fraction achieved through the fabrication method used to produce these inverse PhGs.

Mullite formation took place at 1400 °C, and was promoted by a previous annealing at 850 °C that increased its conversion rate. This proved to be a decisive factor on the structures' dimensional stability at high temperatures.

Considering the notable reflectance performance at temperatures above 1400 °C, we propose integrating these mullite PhGs as a reflective layer in advanced multilayer TBCs. To the best of our knowledge, the maximum operation temperatures achieved by this work are the highest to date for rTBC structures.

Acknowledgements

The authors thank Patrick Udo Kränzien, Dr. Alexander Petrov and Prof. Manfred Eich from the Institute of Optical and Electronic Materials in the Hamburg University of Technology for providing training and access to the ellipsometer and the spectrometer.

Author contributions

Conceptualization, KF; data curation, AG; formal analysis, AG and DRG; Investigation, AG, DRG, TK, LM and BW; project administration, KF; Supervision, KF; resources, KF, MR; visualization, AG and DRG; writing—original draft, AG; writing—review & editing, KF, AG, DRG, TK, LM and BW. All authors have read and agreed to the published version of the manuscript.

Funding

Open Access funding enabled and organized by Projekt DEAL. This work was financially supported by the Deutsche Forschungsgemeinschaft (DFG, German Research Foundation)—Projektnummer 192346071—SFB 986 (project C4 and Z3).

Data availability

The data that support the findings of this study are available from the corresponding author upon reasonable request.

Declarations

Conflict of interest The authors declare that they have no conflict of interest.

Supplementary Information The online version contains supplementary material available at <https://doi.org/10.1007/s10853-023-08844-2>.

Open Access This article is licensed under a Creative Commons Attribution 4.0 International License, which permits use, sharing, adaptation, distribution and reproduction in any medium or format, as long as you give appropriate credit to the original author(s) and the source, provide a link to the Creative Commons licence, and indicate if changes were made. The images or other third party material in this article are included in the article's Creative Commons licence, unless indicated otherwise in a credit line to the material. If material is not included in the article's Creative Commons licence and your intended use is not permitted by statutory regulation or exceeds the permitted use, you will need to obtain permission directly from the copyright holder. To view a copy of this licence, visit <http://creativecommons.org/licenses/by/4.0/>.

References

- [1] Vassen R, Stuke A, Stoeber D (2009) Recent developments in the field of thermal barrier coatings. *J Therm Spray Technol* 18:181–186. <https://doi.org/10.1007/s11666-009-9312-7>
- [2] Soechting FO (1999) A design perspective on thermal barrier coatings. *J Therm Spray Technol* 8:505–511. <https://doi.org/10.1361/105996399770350179>
- [3] Cao XQ, Vassen R, Stoeber D (2004) Ceramic materials for thermal barrier coatings. *J Eur Ceram Soc* 24:1–10. [https://doi.org/10.1016/S0955-2219\(03\)00129-8](https://doi.org/10.1016/S0955-2219(03)00129-8)
- [4] Patnaik P, Huang X, Singh J (2006) State of the art and future trends in the development of thermal barrier coating systems. The NATO Research & Technology Organisation RTO-MP-AVT-135. vol 38, p 1–20
- [5] Kelly MJ, Wolfe DE, Singh J, Eldridge J, Zhu DM, Miller R (2006) Thermal barrier coatings design with increased reflectivity and lower thermal conductivity for high-temperature turbine applications. *Int J Appl Ceram Technol*

- 3:81–93. <https://doi.org/10.1111/j.1744-7402.2006.02073.x>
- [6] Manara J, Arduini-Schuster M, Rätzer-Scheibe HJ, Schulz U (2009) Infrared-optical properties and heat transfer coefficients of semitransparent thermal barrier coatings. *Surf Coat Technol* 203:1059–1068. <https://doi.org/10.1016/j.surfcoat.2008.09.033>
- [7] Lee HS, Kubrin R, Zierold R, Petrov AY, Nielsch K, Schneider GA, Eich M (2012) Thermal radiation transmission and reflection properties of ceramic 3D photonic crystals. *J Opt Soc Am B* 29(3):450–457. <https://doi.org/10.1364/JOSAB.29.000450>
- [8] Singh J, Wolfe DE, Miller RA, Eldridge JI, Zhu DM (2004) Tailored microstructure of zirconia and hafnia-based thermal barrier coatings with low thermal conductivity and high hemispherical reflectance by EB-PVD. *J Mater Sci* 39:1975–1985. <https://doi.org/10.1023/B:JMSS.0000017759.50800.d7>
- [9] Wolfe DE, Singh J, Miller RA, Eldridge JI, Zhu DM (2005) Tailored microstructure of EB-PVD 8YSZ thermal barrier coatings with low thermal conductivity and high thermal reflectivity for turbine applications. *Surf Coat Technol* 190:132–149. <https://doi.org/10.1016/j.surfcoat.2004.04.071>
- [10] Wang L, Eldridge JI, Guo SM (2013) Thermal radiation properties of plasma-sprayed $Gd_2Zr_2O_7$ thermal barrier coatings. *Scr Mater* 69:674–677. <https://doi.org/10.1016/j.scriptamat.2013.07.026>
- [11] Shi H, Zhao CY, Wang BX (2016) Modeling the thermal radiation properties of thermal barrier coatings based on a random generation algorithm. *Ceram Int* 42:9752–9761. <https://doi.org/10.1016/j.ceramint.2016.03.067>
- [12] Ge WA, Zhao CY, Wang BX (2019) Thermal radiation and conduction in functionally graded thermal barrier coatings. Part I: experimental study on radiative properties. *Int J Heat Mass Transf* 134:101–113. <https://doi.org/10.1016/j.ijheatmasstransfer.2019.01.018>
- [13] Yang G, Zhao CY (2015) A comparative experimental study on radiative properties of EB-PVD and air plasma sprayed thermal barrier coatings. *J Heat Transf* 137:091024. <https://doi.org/10.1115/1.4030243>
- [14] Furlan KP, Krekeler T, Ritter M, Blick R, Schneider GA, Nielsch K, Zierold R, Janssen R (2017) Low-temperature mullite formation in ternary oxide coatings deposited by ALD for high-temperature applications. *Adv Mater Interfaces* 4:1700912. <https://doi.org/10.1002/admi.201700912>
- [15] Furlan KP, Larsson E, Diaz A, Holler M, Krekeler T, Ritter M, Petrov AY, Eich M, Blick R, Schneider GA, Greving I, Zierold R, Janssen R (2018) Photonic materials for high-temperature applications: Synthesis and characterization by X-ray ptychographic tomography. *Appl Mater Today* 13:359–369. <https://doi.org/10.1016/j.apmt.2018.10.002>
- [16] Bueno P, Furlan KP, Hotza D, Janssen R (2019) High-temperature stable inverse opal photonic crystals via mullite-sol-gel infiltration of direct photonic crystals. *J Am Ceram Soc* 102:686–694. <https://doi.org/10.1111/jace.16012>
- [17] Kubrin R, Lee HS, Zierold R, Petrov AY, Janssen R, Nielsch K, Eich M, Schneider GA (2012) Stacking of ceramic inverse opals with different lattice constants. *J Am Ceram Soc* 95:2226–2235. <https://doi.org/10.1111/j.1551-2916.2012.05156.x>
- [18] Lee HS, Kubrin R, Zierold R, Petrov AY, Nielsch K, Schneider GA, Eich M (2013) Photonic properties of titania inverse opal heterostructures. *Opt Mater Express* 3:1007–1019. <https://doi.org/10.1364/OME.3.001007>
- [19] Shang G, Dyachenko PN, Leib EW, Vossmeier T, Petrov AY, Eich M (2020) Conductive and radiative heat transfer inhibition in YSZ photonic glass. *Ceram Int* 46:19241–19247. <https://doi.org/10.1016/j.ceramint.2020.04.262>
- [20] Dyachenko PN, Do Rosário JJ, Leib EW, Petrov AY, Kubrin R, Schneider GA, Weller H, Vossmeier T, Eich M (2014) Ceramic photonic glass for broadband omnidirectional reflection. *ACS Photonics* 1:1127–1133. <https://doi.org/10.1021/ph500224r>
- [21] Do Rosário JJ, Dyachenko PN, Kubrin R, Pasquarelli RM, Petrov AY, Eich M, Schneider GA (2014) Facile deposition of YSZ-inverse photonic glass films. *ACS Appl Mater Interfaces* 6:12335–12345. <https://doi.org/10.1021/am502110p>
- [22] Leib EW, Pasquarelli RM, Do Rosário JJ, Dyachenko PN, Doering S, Puchert A, Petrov AY, Eich M, Schneider GA, Janssen R, Weller H, Vossmeier T (2016) Ytria-stabilized zirconia microspheres: novel building blocks for high-temperature photonics. *J Mater Chem C* 4:62–74. <https://doi.org/10.1039/C5TC03260A>
- [23] Do Rosário JJ, Häntsch Y, Pasquarelli RM, Dyachenko PN, Vriend E, Petrov AY, Furlan KP, Eich M, Schneider GA (2019) Advancing the fabrication of YSZ-inverse photonic glasses for broadband omnidirectional reflector films. *J Eur Ceram Soc* 39:3353–3363. <https://doi.org/10.1016/j.jeurceramsoc.2019.04.028>
- [24] Campos HG, Furlan KP, Garcia DE, Blick R, Zierold R, Eich M, Hotza D, Janssen R (2019) Effects of processing parameters on 3D structural ordering and optical properties of inverse opal photonic crystals produced by atomic layer deposition. *Int J Ceramic Eng Sci* 1:68–76. <https://doi.org/10.1002/ces2.10015>
- [25] Pasquarelli RM, Lee HS, Kubrin R, Zierold R, Petrov AY, Nielsch K, Schneider GA, Eich M, Janssen R (2015) Enhanced structural and phase stability of titania inverse

- opals. *J Eur Ceram Soc* 35:3103–3109. <https://doi.org/10.1016/j.jeurceramsoc.2015.04.041>
- [26] Zhou Z, Zhao XS (2005) Opal and inverse opal fabricated with a flow-controlled vertical deposition method. *Langmuir* 21:4717–4723. <https://doi.org/10.1021/la046775t>
- [27] Gomez-Gomez A, Winhard B, Lilleodden E, Huber N, Furlan KP (2022) Unravelling the role of shell thickness and pore size on the mechanical properties of ceramic-based microporous structures. *J Am Ceram Soc* 106:1273–1286. <https://doi.org/10.1111/jace.18811>
- [28] Schulz U (2000) Phase transformation in EB-PVD yttria partially stabilized zirconia thermal barrier coatings during annealing. *J Am Ceram Soc* 83:904–910. <https://doi.org/10.1111/j.1151-2916.2000.tb01292.x>
- [29] Leib EW, Pasquarelli RM, Blankenburg M, Schreyer A, Janssen R, Weller H, Vossmeier T (2016) High-temperature stable zirconia particles doped with yttrium, lanthanum, and gadolinium. *Part Part Syst Charact* 33:645–655. <https://doi.org/10.1002/ppsc.201600069>
- [30] Sévin L, Audouard L, Razafindramana V, Mauvy F, Galzin L, Justin JF, Bertrand P, Langlade C, Garcia M, Julian-Jankowiak A (2023) Phase stabilisation, thermal expansion and ionic conductivity of high content rare earth oxide (Lu_2O_3 , Y_2O_3 and Gd_2O_3) stabilised cubic hafnia. *J Eur Ceram Soc* 43:4153–4166. <https://doi.org/10.1016/j.jeurceramsoc.2023.03.006>
- [31] Pan L, He L, Niu Z, Xiao P, Zhou W, Li Y (2023) Corrosion behavior of ytterbium hafnate exposed to water-vapor with $\text{Al}(\text{OH})_3$ impurities. *J Eur Ceram Soc* 43:612–620. <https://doi.org/10.1016/j.jeurceramsoc.2022.09.013>
- [32] Ramaswamy P, Seetharamu S, Varma KBR, Rao KJ (1998) Thermal shock characteristics of plasma sprayed mullite coatings. *J Therm Spray Technol* 7:497–504. <https://doi.org/10.1361/105996398770350710>
- [33] Kokini K, Takeuchi YR, Choules BD (1996) Surface thermal cracking of thermal barrier coatings owing to stress relaxation: zirconia versus mullite. *Surf Coat Technol* 82:77–82. [https://doi.org/10.1016/0257-8972\(95\)02647-9](https://doi.org/10.1016/0257-8972(95)02647-9)
- [34] Aksay IA, Dabbs DM, Sarikaya M (1991) Mullite for structural, electronic, and optical applications. *J Am Ceram Soc* 74:2343–2358. <https://doi.org/10.1111/j.1151-2916.1991.tb06768.x>
- [35] Duval DJ, Risbud SH, Shackelford JF (2008) Mullite. In: Shackelford JF, Doremus RH (eds) *Ceramic and glass materials: structure, properties and processing*. Springer, Boston, pp 27–39. https://doi.org/10.1007/978-0-387-73362-3_2
- [36] Ruiz de Sola E, Torres FJ, Alarcón J (2006) Thermal evolution and structural study of 2:1 mullite from monophasic gels. *J Eur Ceram Soc* 26:2279–2284. <https://doi.org/10.1016/j.jeurceramsoc.2005.04.015>
- [37] Cividanes LS, Campos TMB, Rodrigues LA, Brunelli DD, Thim GP (2010) Review of mullite synthesis routes by sol-gel method. *J Sol-Gel Sci Technol* 55:111–125. <https://doi.org/10.1007/s10971-010-2222-9>
- [38] Wang K, Sacks MD (1996) Mullite formation by endothermic reaction of α -alumina/silica microcomposite particles. *J Am Ceram Soc* 79:12–16. <https://doi.org/10.1111/j.1151-2916.1996.tb07874.x>
- [39] Galisteo-López JF, Ibisate M, Sapienza R, Froufe-Pérez LS, Blanco A, López C (2011) Self-assembled photonic structures. *Adv Mater* 23:30–69. <https://doi.org/10.1002/adma.201000356>
- [40] Armstrong E, O'Dwyer C (2015) Artificial opal photonic crystals and inverse opal structures—fundamentals and applications from optics to energy storage. *J Mater Chem C* 3:6109–6143. <https://doi.org/10.1039/C5TC01083G>
- [41] Do Rosário JJ, Berger JB, Lilleodden E, McMeeking RM, Schneider GA (2017) The stiffness and strength of metamaterials based on the inverse opal architecture. *Extreme Mech Lett* 12:86–96. <https://doi.org/10.1016/j.eml.2016.07.006>
- [42] García PD, Sapienza R, Blanco A, López C (2007) Photonic glass: a novel random material for light. *Adv Mater* 19:2597–2602. <https://doi.org/10.1002/adma.200602426>
- [43] Ogurreck M, Do Rosário JJ, Leib EW, Laipple D, Greving I, Marschall F, Last A, Schneider GA, Vossmeier T, Weller H, Beckmann F, Müller M (2016) Determination of the packing fraction in photonic glass using synchrotron radiation nanotomography. *J Synchrotron Rad* 23:1440–1446. <https://doi.org/10.1107/S1600577516012960>
- [44] García PD, Sapienza R, Bertolotti J, Martín MD, Blanco A, Altube A, Viña L, Wiersma DS, López C (2008) Resonant light transport through Mie modes in photonic glasses. *Phys Rev A* 78:023823. <https://doi.org/10.1103/PhysRevA.78.023823>
- [45] Schertel L, Siedentop L, Meijer JM, Keim P, Aegerter CM, Aubry GJ, Maret G (2019) The structural colors of photonic glasses. *Adv Optical Mater* 7:1900442. <https://doi.org/10.1002/adom.201900442>
- [46] Chen J, Wheeler VM, Liu B, Kumar A, Coventry J, Lipski W (2021) Optical characterisation of alumina-mullite materials for solar particle receiver applications. *Sol Energy Mater Sol Cells* 230:111170. <https://doi.org/10.1016/j.solmat.2021.111170>
- [47] Chen P, Xiao P, Tang X, Li Y (2022) Corrosion behavior and failure mechanism of SiC whisker and c-ALPO4 particle-modified novel tri-layer $\text{Yb}_2\text{Si}_2\text{O}_7$ /mullite/SiC coating

in burner rig tests. *J Adv Ceram* 11:1901–1917. <https://doi.org/10.1007/s40145-022-0655-6>

- [48] Wahl FM, Grim RE, Graf RB (1961) Phase transformations in silica as examined by continuous x-ray diffraction. *Am Mineral* 46:196–208
- [49] Zheng W, Chen X, Liu C, Ren S, Zhang L (2021) Effects of micro-sized mullite on cristobalite crystallization and properties of silica-based ceramic cores. *Int J Appl Ceram Technol* 18:1244–1254. <https://doi.org/10.1111/ijac.13769>
- [50] Chen X, Liu C, Zheng W, Han J, Zhang L, Liu C (2020) High strength silica-based ceramics material for investment casting applications: effects of adding nanosized alumina

coatings. *Ceram Int* 46:196–203. <https://doi.org/10.1016/j.ceramint.2019.08.248>

- [51] Wei WC, Halloran JW (1988) Transformation kinetics of diphasic aluminosilicate gels. *J Am Ceram Soc* 71:581–587. <https://doi.org/10.1111/j.1151-2916.1988.tb05923.x>

Publisher's Note Springer Nature remains neutral with regard to jurisdictional claims in published maps and institutional affiliations.